Macalester Journal of Physics and Astronomy

Volume 7
Issue 1 *Spring 2019*

Article 3

Recent Evolution of the Eta Carinae Supernova Imposter System

Greta L. Helmel
Macalester College, ghelmel@macalester.edu

Abstract

The supernova imposter Eta Carinae and its surrounding Homunculus reflection nebula have been of great interest for the last several decades. As the most massive star known in our Galaxy, this object is of particular importance in understanding high mass loss episodes and final stages in the evolution of other similarly massive stars in the later stages of their lives. Observations using the STIS CCD Instrument have been taken over the past 20 years for both the central star and the Homunculus as part of the *Hubble Space Telescope* (*HST*) Treasury Program on Eta Carinae. Recent changes in the spectra of the star from 2012 to 2018 confirm the continuation of certain trends in the star's behavior, including both an overall brightening and the related decrease in the stellar wind density. Around 2004, Eta Carinae began a period of rapid change, where major stellar wind emission features decreased by factors of 2-4 over the rest of the decade. Here we find that this dramatic development seems to have slowed over the last 6 years, implying that the mass loss rate has not changed significantly since 2010; these findings are consistent over all visible wavelength regions available in our observations.

In addition to probing the behavior of the central star, we also consider the development of the Homunculus nebula over the past 18 years, using intensity tracings of the line-free continuum in order to determine a precise expansion rate of 11.9% ± 0.1% between the two epochs of March 2000 and February 2018. This is one of the longest baselines ever produced for this object using a single instrument. This expansion rate yields an ejection date (assuming ballistic motion) of 1849.2 ±1.7 yr, which is in good agreement with other recent studies. We also consider the change in brightness of the nebula over this baseline.

Recent Evolution of the Eta Carinae Supernova Imposter System

Cover Page Footnote
Work on the central star was completed as a part of the summer 2018 University of Minnesota Physics and Astronomy REU Program, funded by the National Science Foundation. This work has made use of the data archive for Eta Carinae, which is available online at http://etacar.umn.edu. The archive is supported by the University of Minnesota and the Space Telescope Science Institute under contract with NASA.

MACALESTER COLLEGE

Recent Evolution of the Eta Carinae Supernova Imposter System

by

Greta Helmel

in the

Department of Physics and Astronomy

Advisor: John Cannon

May 2019

MACALESTER COLLEGE

Abstract

Department of Physics and Astronomy

by Greta Helmel

The supernova imposter Eta Carinae and its surrounding Homunculus reflection nebula have been of great interest for the last several decades. As the most massive star known in our Galaxy, this object is of particular importance in understanding high mass loss episodes and final stages in the evolution of other similarly massive stars in the later stages of their lives. Observations using the STIS CCD Instrument have been taken over the past 20 years for both the central star and the Homunculus as part of the *Hubble Space Telescope (HST)* Treasury Program on Eta Carinae. Recent changes in the spectra of the star from 2012 to 2018 confirm the continuation of certain trends in the star's behavior, including both an overall brightening and the related decrease in the stellar wind density. Around 2004, Eta Carinae began a period of rapid change, where major stellar wind emission features decreased by factors of 2-4 over the rest of the decade. Here we find that this dramatic development seems to have slowed over the last 6 years, implying that the mass loss rate has not changed significantly since 2010; these findings are consistent over all visible wavelength regions available in our observations.

In addition to probing the behavior of the central star, we also consider the development of the Homunculus nebula over the past 18 years, using intensity tracings of the line-free continuum in order to determine a precise expansion rate of 11.9% ± 0.1% between the two epochs of March 2000 and February 2018. This is one of the longest baselines ever produced for this object using a single instrument. This expansion rate yields an ejection date (assuming ballistic motion) of 1849.2 ±1.7 yr, which is in good agreement with other recent studies. We also consider the change in brightness of the nebula over this baseline.

Acknowledgements

I have to start by expressing my deepest gratitude to my Macalester advisor, John Cannon, for all of your guidance and advice over the past three years. You offered me my first opportunity to engage in research and understand just how wonderful it is to get to do something real and to understand the universe a little bit more. A wealth of thanks is also due to the advisors for this project, Roberta Humphreys and Kris Davidson, who not only took me on for summer 2018, but allowed me to continue this work into the following semesters. Thank you for your patience and guidance throughout this project. I also want to thank Will Mitchell for your help deciphering the math behind the science, as well as Anna Williams and Michael Wood, for serving on my review committe and for your thorough, thoughtful feedback on this work.

Thank you to my family, my partner Elliot, and my friends in the Physics department and beyond; I wouldn't have made it through all of this if it weren't for you folks. Your support, compassion, patience, and commiseration throughout these four years has meant the world to me. A special thanks is due to Lilly, my housemate and Python Jedi master; without you, these figures would never have looked as nice as they do, and my sanity would have looked worse. I love you all.

Finally, thank you to Eta Carinae for putting the "super no" in supernova. What a star.

Contents

List of Figures

List of Tables

CHAPTER 1: Introduction

1.1 Overview

This thesis discusses the recent evolution of the system of Eta Carinae (Eta Car), a closely studied giant eruption luminous blue variable (LBV) and "supernova imposter." The supernova imposter phenomenon refers to the fact that in the 1840s, Eta Car underwent a nonterminal explosion in which great amounts of matter were ejected, forming the Homunculus nebula that surrounds it. Eta Car has continued to evolve since then, and still has not recovered from its "Great Eruption." Eta Car is of particular scientific interest in that it is the only object of this type close enough to study in detail; as such, one of the most critical means of understanding this object and others like it is to study the trends in its behavior over time. To that end, we present and analyze spectra taken as a part of the *Hubble Space Telescope (HST)* Treasury Program on Eta Carinae, both for the central star and the surrounding Homunculus. We use these to probe various conditions and behaviors of the system, comparing our results to previous work in order to track its evolution over the twenty years it has been observed with these methods.

This chapter provides an overview of the Eta Car system, as well as a discussion of the previous work that has motivated and provided the foundation for ours. Chapter 2 describes the spectral data and methods used to extract the relevant data products. Chapter 3 presents analysis specific to the central star, including the brightness of the continuum, evolution of absorption and emission features across various wavelength regions, and an estimation of the change in the mass loss rate over the last 6 years. Analysis of the Homunculus nebula, including the brightness, expansion rate, and a new estimate of the nebula's age are given in Chapter 4. Conclusions and suggestions for future work are made in Chapter 5.

1.2 Motivations

In the last decade, Mehner et al. (2010b) identified what they referred to as a "Sea Change" in the behavior of Eta Car's stellar wind. The equivalent width measurements on various emission features from this region saw dramatic changes on very short timescales; features at the same phase[1] decreased by factors of 2-4 (Mehner et al. 2010b, see Figure 1.1). This had significant implications for the mass loss rate and wind density of the star, suggesting that the density was decreasing rapidly and the mass loss rate was decreasing over time as well. This was confirmed in part by Mehner et al. (2012), which found rough estimates of the mass loss rate to have declined by a factor of 2-3 between 1999 and 2010.

Both studies, as well as this thesis, make use of the Treasury Program on Eta Car that began in 1998, which populates a rich collection of spectra contained in the online Eta Carinae Data Archive.[2] The newest dataset acquired in February 2018 offered an opportunity to investigate whether this rapid development had continued or if instead the behavior had undergone yet another change.

Other overarching studies have been published since the Sea Change was identified (Mehner et al. 2012; Davidson et al. 2018, etc), but none have covered the most recently acquired data directly comparable to the Sea Change; that is, the secular changes in features of the visible wavelength regime. Although we also acquired UV data for this cycle, analysis of these are left for future studies, the reasoning behind which is discussed further in Chapter 3.

In addition to looking at the central star, the February 2018 observations also covered some spectral regions for the Homunculus nebula. With this new dataset, we now have an 18-year baseline of spectra for the Homunculus that have been taken on the same instrument under identical observing conditions. This gives us the opportunity to study the nature of the changes—specifically, the expansion—of the ejected material using one of the longest baselines ever acquired for this object. From these data, we can determine a wealth of characteristics for the Homunculus, including the change in brightness over time, the expansion rate of

[1] See section 2.1 for a discussion of phase.
[2] Archive can be accessed at http://etacar.umn.edu/archive.

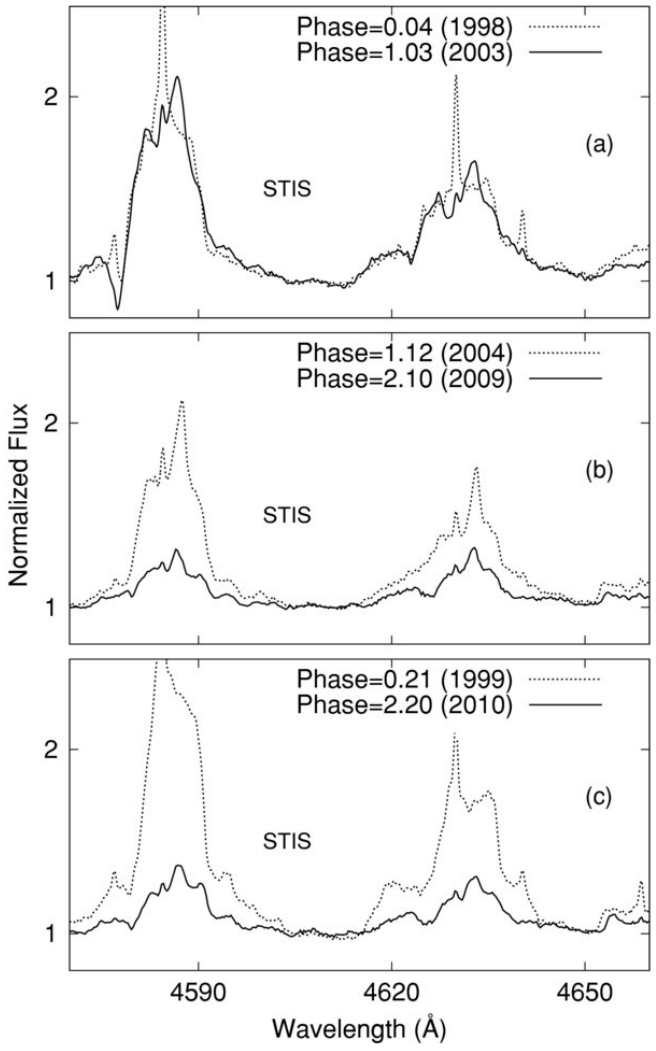

FIGURE 1.1: Eta Carinae's "Sea Change," exemplified by blends of Fe II, [Fe II], Cr II, and [Cr II] near 4600 Å. Adapted from Figure 1 in Mehner et al. (2010b). Prior to 2004, changes in the emission features of Eta Car were slow and minimal (a). However, between 2004 and 2010, (b) and (c) show dramatic changes in which the features decrease by factors of 2-4. This corresponds to a rapid decrease in the stellar wind density and accordingly, a decrease in the mass loss rate for the star.

the ejected material, and from the expansion rate, an estimate of the age of the nebula.

Historically, Eta Car's Great Eruption has been temporally located in the early 1840's due to brief periastron luminosity spikes in 1843 (Smith & Frew 2011; Davidson & Humphreys 2012); however, recent studies with greater precision have placed the ejection date of the bulk the nebula to be around 1847 (Morse et al.

2001; Smith 2017). Comparing with these studies is of particular interest, since they have similar robustness but use different methods and instruments on the *HST* from our data. This provides a useful check for systematic error and corroborates the results we obtain.

Because Eta Car is relatively close and therefore easy to observe in detail, it is important to track its behavior in a consistent way, as doing so will provide insight into its current instability and recovery from the Great Eruption, its further evolution, and eventual death. Understanding this system will provide valuable insight into high mass loss events, non-terminal eruptions, and the late-stage evolution of other extremely massive stars, such as the five potential analogs recently discovered in nearby galaxies (Khan et al. 2015).

1.3 The Eta Carinae / Homunculus Nebula System

Eta Carinae is understood to be a binary star system, though we have never observed either star directly due to the surrounding dense material of the Homunculus nebula, as seen in Figure 1.2 (Damineli et al. 1997; Gull 2007; Damineli 2008). In spite of this, overwhelming evidence exists for Eta Car's binary partner, which has been estimated to have $M_{ZAMS} \sim$ 40-50 $M_\odot$ and L $\sim 4{\times}10^5$ $L_\odot$(Mehner et al. 2010a). The orbit of the binary is highly eccentric, with e $\gtrsim$ 0.85 (Kashi & Soker 2010; Davidson & Humphreys 2012). The semimajor axis of the system is estimated to be ∼17 AU (Martin et al. 2010). Properties for the primary star, which dwarfs the already extremely massive secondary, are reported in Table 1.1.

One of the strongest pieces of evidence for a binary partner is the 5.54 year spectroscopic cycle over which the emission and absorption features of Eta Car's solar wind vary with the orbital motion of the secondary star. At periastron, the secondary star dives through and disturbs the stellar wind of the primary star, causing high excitation emission lines to weaken or disappear completely in so-called 'spectroscopic events' (Martin et al. 2006a; Damineli 2008; Davidson & Humphreys 2012, and many references therein). A history of these spectroscopic events from the

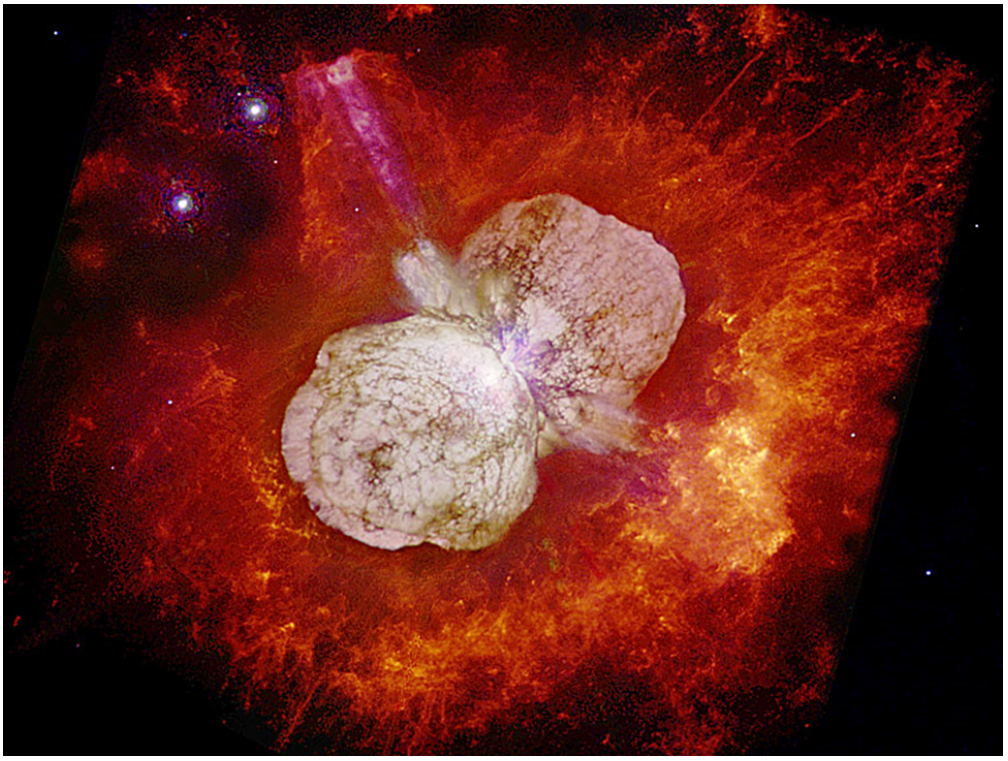

FIGURE 1.2: Composite *HST*/WFPC2 high resolution imaging of Eta Carinae and the Homunculus Nebula (N. Smith, J. A. Morse (U. Colorado) et al., NASA). Field of view is approximately 38 x 33 arcseconds (Morse et al. 1998).

Property	Value
Right Ascension	161.2650833°
Declination	-59.6844723°
Luminosity	$\sim 5\times10^6$ $L_\odot$ [a]
Mass	$\geq\sim$120 $M_\odot$ [a]
Mass Loss Rate	$\sim 10^{-3}$ $M_\odot$/yr [b]
Adopted Distance	2300 $\pm$ 50pc [a]

TABLE 1.1: Current Properties of Eta Carinae's Primary Star.
[a] Davidson & Humphreys (2012)
[b] Hillier et al. (2001); Mehner et al. (2012)

late 1940s to the most recent event in mid-2014 can be found in Mehner et al. (2015). Various wind models such as that in Figure 1.3 have been proposed for the ionization zones and regions of the primary's wind at various points in the secondary's orbit, but almost all of them are highly simplified and idealized, given the complexity of the system and inability to observe it directly (Martin et al. 2006a; Mehner et al. 2011). Different emission features arise from different regions

of the wind; for instance, much of the N II absorption lines are expected to arise from zone 1 in Figure 1.3 (Mehner et al. 2011).

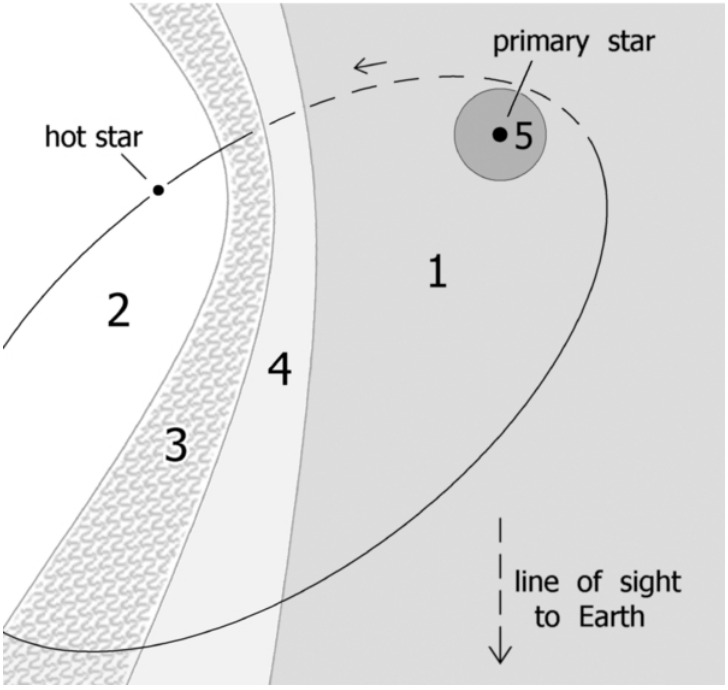

FIGURE 1.3: This figure from Mehner et al. (2011) shows a typical (highly simplified) wind model for the system shortly after the 2009 periastron event. The area shown is approximately 25 AU across. Numbers on the figure represent zones of the stellar wind; regions 1 and 5 are undisturbed parts of the primary's wind, while region 2 is the secondary's significantly less dense wind. Region 3 is the complex shocked wind-wind collision region, and region 4 is a He II zone photoionized by the secondary star (Mehner et al. 2011, 2012).

Less than 0.3 arcseconds from the central star are three bright condensations of ejected material referred to as the "Weigelt knots," which were first discovered using speckle interferometry; see Figure 1.4 (Weigelt & Ebersberger 1986; Hofmann & Weigelt 1988). These knots are moving outwards at less than 50 km/s, and are thought to have been ejected at some point during Eta Carinae's second, lesser eruption around 1890 (Davidson & Humphreys 2012). It was not until the *HST* became available that spectra uncontaminated by the knots were able to be obtained; at the time of writing, *HST* remains the only instrument with enough resolving power to separate out the emission from just the star (see Section 2.1 for further discussion).

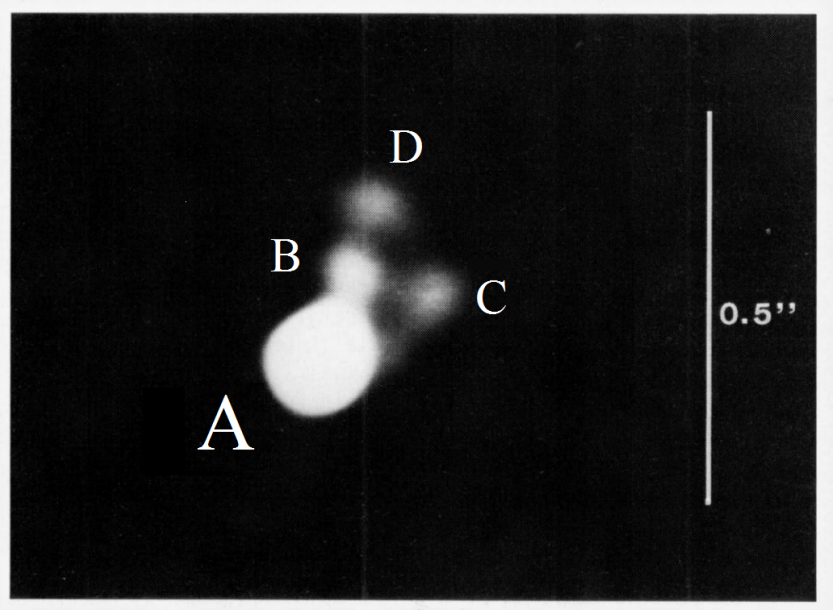

FIGURE 1.4: 850 nm speckle masking observation of Eta Carinae's Weigelt knots, taken with the 2.2-m ESO/MPG telescope. The central star is labeled as A, while the three Weigelt knots B, C, and D are marked accordingly. As shown by the scale, these knots are extremely close in angular separation to the star, and as such contaminate all current ground based-spectra of Eta Car (see Section 2.1 for further discussion). As per convention, north is top, east is left. Figure adapted from Hofmann & Weigelt (1988).

The Homunculus reflection nebula formed during the primary star's Great Eruption in the 1840s, which expelled ∼12 $M_\odot$ of material from the star (Smith 2008). The mechanisms that caused this eruption are likely related to the Eddington limit of the star, and was possibly provoked in some way by the secondary binary partner (Kashi & Soker 2010; Davidson & Humphreys 2012). In 2003, Ishibashi et al. (2003) reported the discovery of a second, smaller nebular structure embedded within the greater Homunculus, appropriately deemed the "Little Homunculus." This structure is understood to be younger than the Homunculus, likely a result of Eta Car's lesser eruption (Ishibashi et al. 2003). Both the Homuculus nebula and the embedded Little Homunculus appear to be almost hollow; that is to say that though there is some low density material within them, the shell surfaces of the nebulae are well defined (see references in Ishibashi et al. 2003). The outer ejecta surrounding the Homunculus, clearly visible in Figure 1.2 as the diffuse reddish material, is thought to be the result of various ancient ejections both predating and coinciding with the Great Eruption of the 1840s (Kiminki et al. 2016).

CHAPTER 2: Data and Extraction Methods

2.1 Central Star Data

Eta Car's Weigelt knots—bright ejected gas only 0.3 arcseconds away from the primary star—necessitate using a telescope with enough resolving power to separate out emission from only the star. All ground-based spectroscopy invariably includes contamination from the knots (see Figure 2.1).

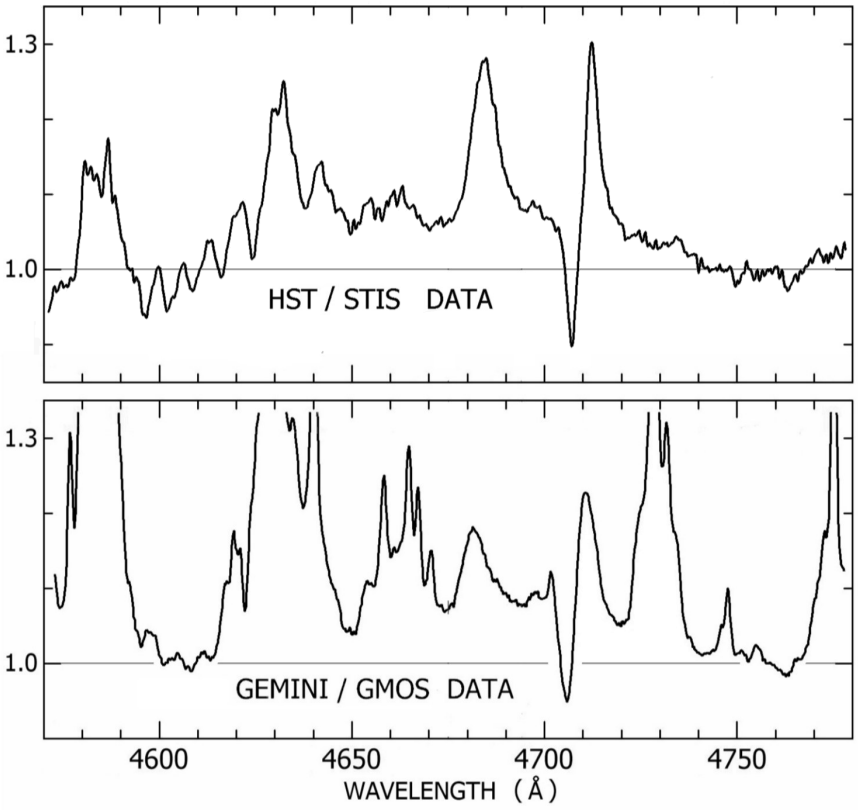

FIGURE 2.1: Comparison of an *HST* spectrum vs a ground-based Gemini spectrum, the latter of which has a seeing-limited resolution of 0.5 - 2.0 arcseconds; this necessarily includes spectral contamination from the Weigelt knots. Gemini spectra have a slit position correction applied as described by Martin and Mehner in Technical Memo 14 of the *HST* Treasury Program archive.[1] The Gemini/GMOS slit size is 0.5 arcseconds, compared to 0.1 arcseconds of the *HST*/STIS slit used for our data. (Figure adapted from Davidson et al. 2015, courtesy of http://etacar.umn.edu)

As such, the spectra presented and analyzed here were taken with the *Hubble Space Telescope*'s Space Telescope Imaging Spectrograph (STIS) CCD instrument. The STIS CCD spectra are reduced and flux-calibrated through the CALSTIS pipeline before being included in the Eta Car *HST* Treasury Program Archive. They have a resolution of 0.0253 arcseconds/pixel, and cover a wavelength range of 1700 - 10000 Å (see Figure 2.2). We disregard the position angle of the telescope for these spectra, as we extract only the innermost region that is centered on the star, as described in section 2.1.1.

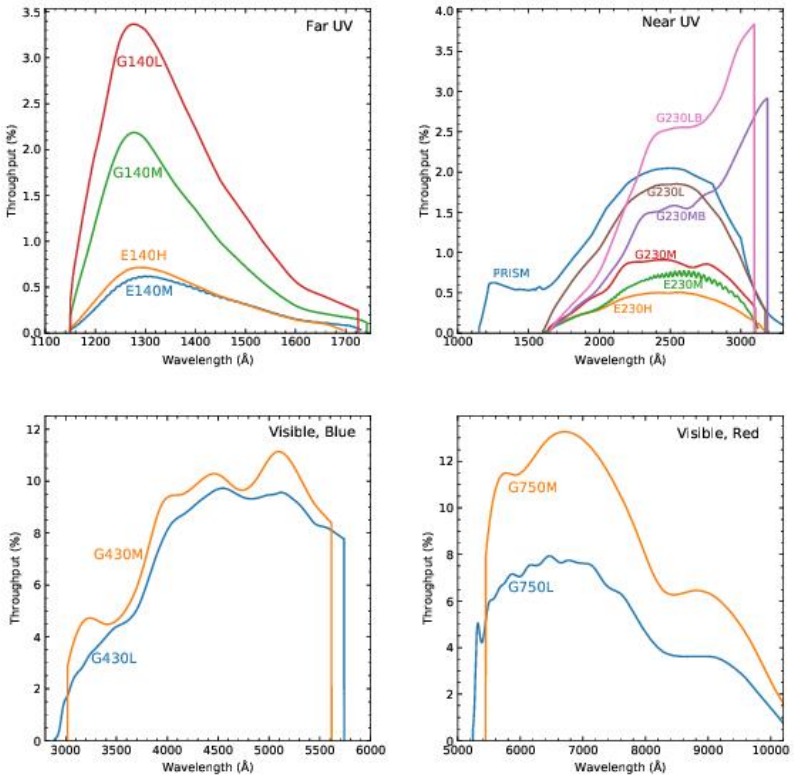

FIGURE 2.2: STIS Instrument system throughputs for various grating modes from Hernandez & et al. (2012). The data considered in this work uses the STIS optical elements G750M and G430M.

As discussed in Section 1.3, emission lines from Eta Car weaken and vanish during 5.54 year spectroscopic events in which the binary passes through periastron (Mehner et al. 2010b). In order to best quantify changes over time in the spectra of Eta Carinae, we compare spectra from corresponding phases in each cycle. "Phase" is defined here as in the Eta Car *HST* Treasury Program Archive, where

P = 2023.0 days, and t_0 = MJD 50814.0 = J1998.00 (marking the first spectroscopic event observed by STIS). Phases 0.00, 1.00, etc., mark the spectroscopic events of 1998.0, 2003.5, and so on. The integer value represents the number of cycles since 1998.0, while the decimal value gives the phase of the secondary star.

The most recent observations were taken February 22nd, 2018, corresponding to phase 3.63652. For the central star, we compare these newest spectra to observations taken October 19th, 2012 (phase 2.67152) and in a few specific areas of interest, October 1st, 2001 (phase 0.67679). There is no data at this phase from the second cycle (cycle 1), as the STIS instrument was inoperative during this time. For most of the comparisons, we are primarily interested in the recent changes; that is, any developments since cycle 2. All of the data considered in this work for the central star is in the visible wavelength region, using the STIS optical elements G750M and G430M, with the 52" x 0.1" slit.

2.1.1 Stellar Spectra Extraction Methods

I used the `exfits` program developed at the University of Minnesota by Matt Gray and John Martin in order to extract one-dimensional spectra of the star. This program utilizes subpixel modelling to extract a 1D spectral tracing from 2D FITS files. First the `trace` function was used to find the center of the spectrum (i.e., the star), which was verified visually via the 2D spectra in SAOImage DS9. This center pixel value was then used in a row-based mesa extraction with a base of 7 pixels and peak of 5 pixels. The "mesa" refers to the shape of the sampling function that we use along the spectrograph slit, which blurs the edges of the sampling function by the base value, therefore reducing the pixelization. Our choice of peak value corresponds to an extraction width of 0.127", and selects just the emission from the star.

2.2 Homunculus Nebula Data

For the surrounding Homunculus nebula, our goals were different in that we wished to probe the expansion behavior and brightness over the nearly two decades it

has been covered by *HST*/STIS. As such, we compare the newest February 2018 STIS/CCD spectra to spectra taken March 13, 2000. For these observations, the central star was occulted on the slit to obtain spectra of the relatively fainter surrounding nebula. The relevance of various observing parameters is opposite to that which we applied to the spectra of the central star; here, we disregard the phase of the central binary, and instead, require that we have the same position angle so as to capture the same slice of nebular material. For both epochs, the position angle is -42.497° (see Figure 2.3 for slit orientation across the nebula), and the optical element used was G750M, with the 52" x 0.2" slit.

We chose to use the wavelength region centered at 6768 Å for our continuum estimate because of the long exposure times and relative lack of emission or absorption features (that is, the strength and lack of contamination of the continuum). The Hα line is saturated in both spectra, but since we are interested in the continuum, this is irrelevant, and the deeper exposure time is necessary to see the significantly fainter nebula.

2.2.1 Homunculus Continuum Extraction Methods

Since our intention for the nebula was to look at the continuum rather than to investigate changes in equivalent widths of specific features in the same way as for the star, we extracted the data accordingly. First, I identified wavelength ranges within the spectra that had little to no emission lines present—i.e., the continuum. I selected five such regions ranging in width from 28 - 40 Å (∼130 pixels average; see Figure 2.4 for the cuts). I then took a one-dimensional cut of that region using `exfits`, this time using a column-based square extraction that averages the intensity values for each row across the wavelength columns. The detector is oriented such that high row numbers in the resulting 1D tracings correspond to the northwest lobe of the nebula, and low to the southeast.

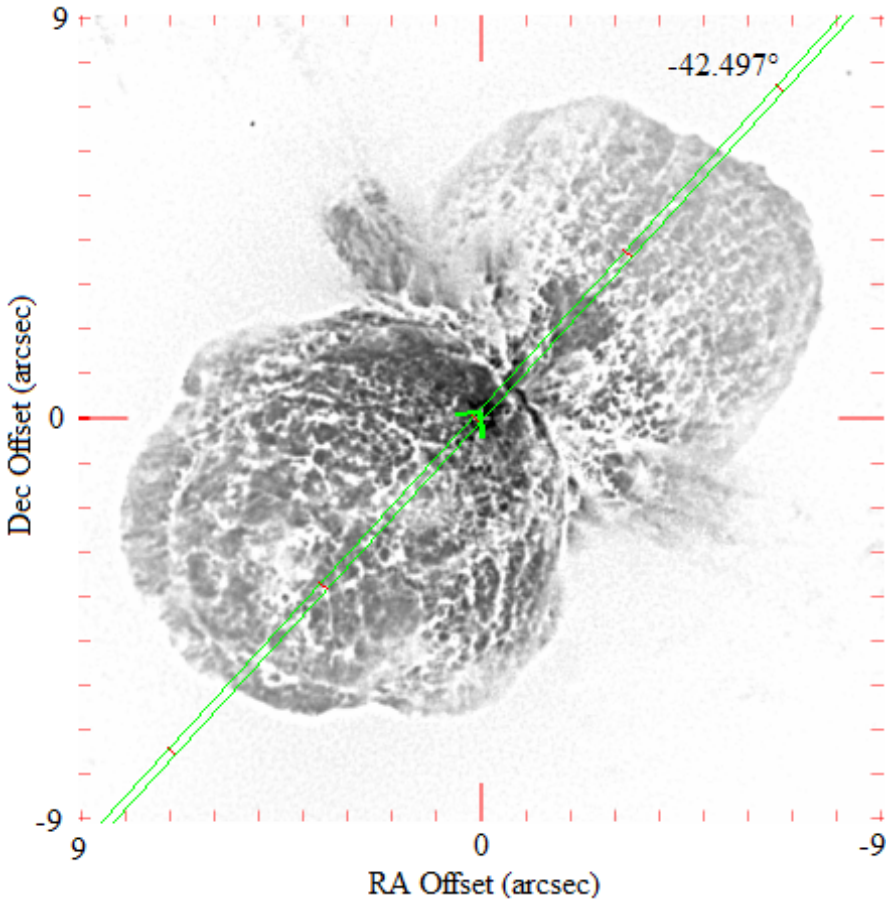

FIGURE 2.3: 1995 *HST*/WFPC2 image of the Homunculus Nebula, overlain with a slit showing the position angle (-42.497°) of the spectra from both epochs. The (0,0) position is the location of the central star, whose RA and Dec coordinates are listed in Table 1.1.

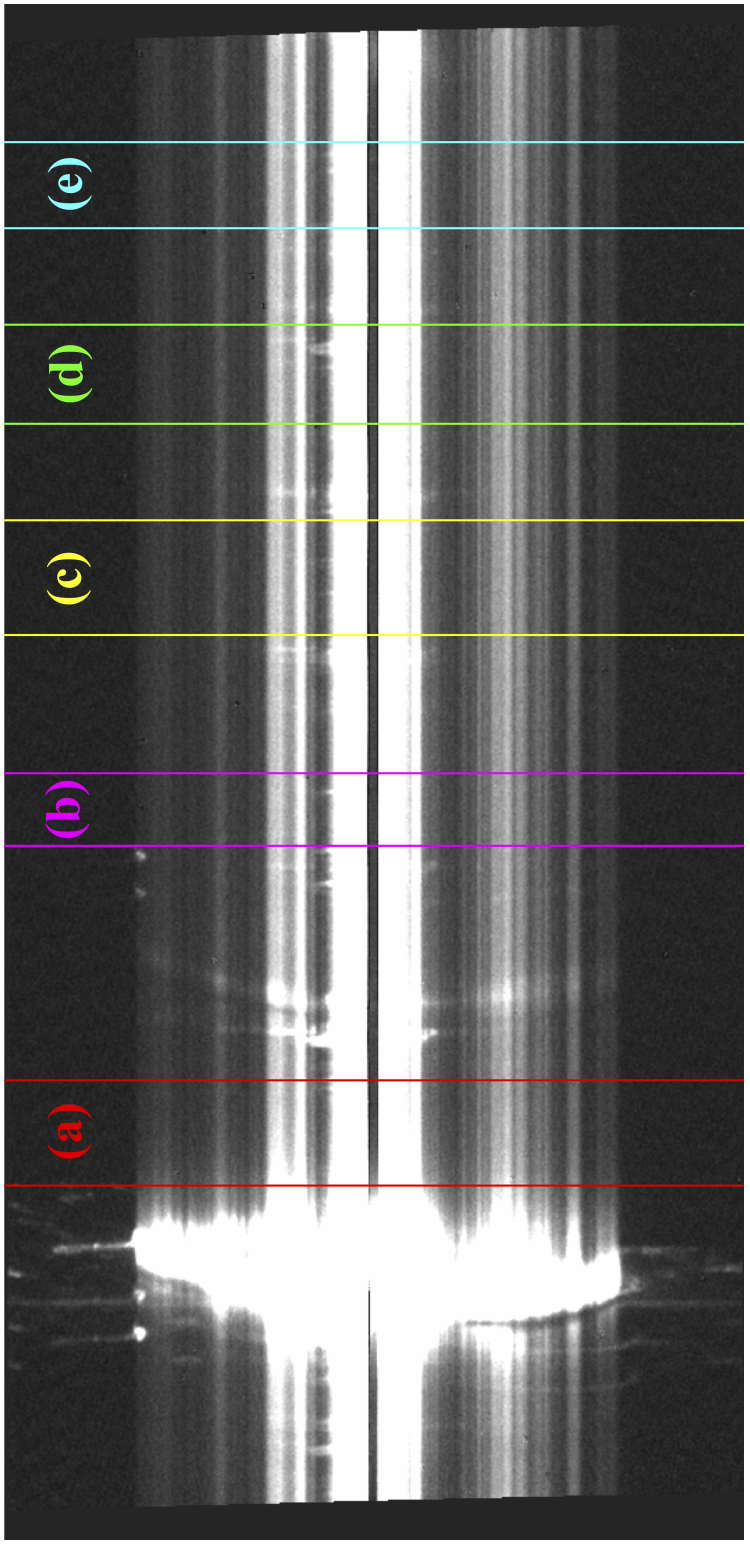

FIGURE 2.4: Wavelength regions used for intensity tracing extractions of the Homunculus nebula, overlain on the March 2000 2D FITS spectrum. The horizontal axis represents wavelength, while the vertical axis is the position along the slit (represented by a row number given in pixels). Regions were chosen based on the relative lack of emission or absorption features, since we are trying to probe the continuum of the nebula. Wavelength ranges are as follows: (a) $\lambda\lambda$6610 to 6650, (b) $\lambda\lambda$6740 to 6768, (c) $\lambda\lambda$6821 to 6865, (d) $\lambda\lambda$6902 to 6940, and (e) $\lambda\lambda$6977 to 7010.

CHAPTER 3: Eta Carinae

3.1 Continuum Brightening of Central Star

Overall, the continuum flux level of the central star has brightened over time across all regions (see for example Figure 3.1). This is expected, given the decrease in the primary wind density indicated by the trends of the emission lines over time (Mehner et al. 2010b, 2012); that is to say, if the density of the wind is decreasing, then more light from the star is able to escape, and the star brightens to us as observers.

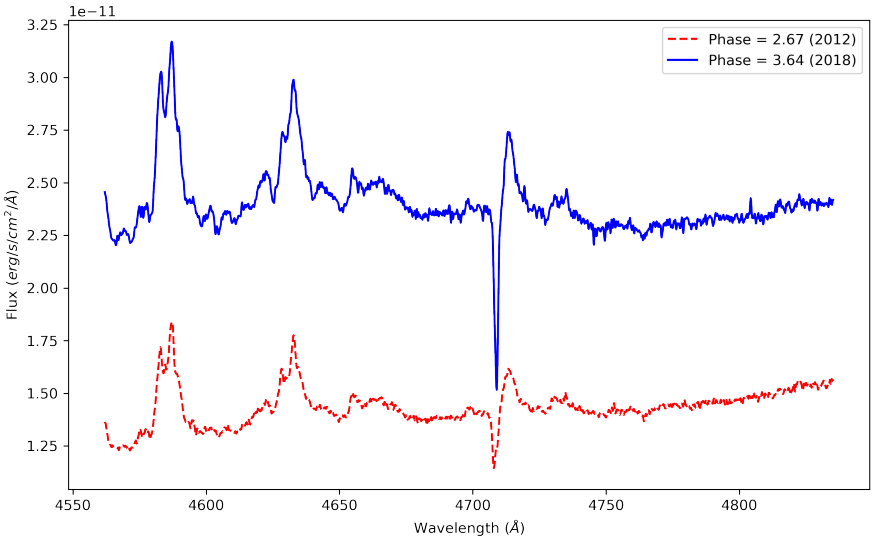

FIGURE 3.1: Continuum flux level increase for the primary star from 2012 to 2018 is evident across all visible wavelength regions; part of the λ4561 to λ4841 region is shown here as an example. No artificial displacement has been added. This shows a clear continuation of the brightening of the primary star, a trend that has been observed over time due to the expansion of the nebula and the decrease in the stellar wind density.

To further illustrate this point, Figure 3.2 shows the percent increase in the average continuum level for each visual wavelength region studied. The star has brightened across all of these regions, though we notice a slight decreasing trend towards the redder wavelengths. Being that a significant part of this brightness increase is likely due to dust destruction and the expansion of the nebula, which necessarily

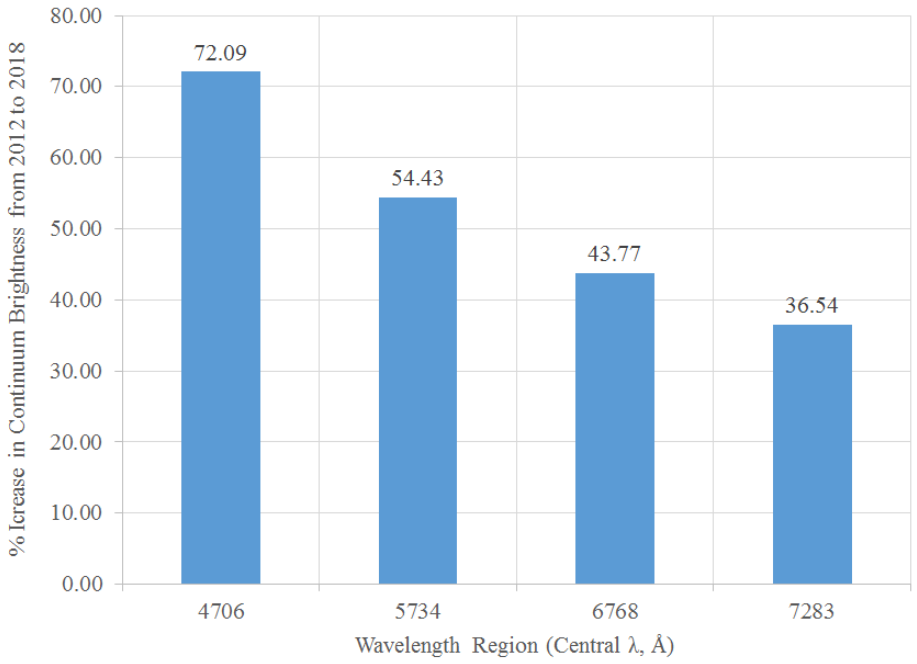

FIGURE 3.2: Percent increase in brightness of the central star from 2012 to 2018, based on the average continuum flux level measured for each wavelength region at each epoch. Regions are identified by their central wavelength. The star has brightened significantly across all four regions.

reddens the star, it is logical that the star increases more in the bluer wavelengths as the visibility increases. Evidence for the weakening of the dust opacity has indeed been observed in the mid-IR (Morris et al. 2017). Most often the overall brightness level of the star is quantified using the UV regions; see section 3.2.5 for further discussion thereof.

3.2 Spectral Line Changes

I analyzed various spectral features in four visible wavelength regions, analogous to the procedures in Mehner et al. (2010b). Below is a complete consideration of the features analyzed, including equivalent widths of notable emission and absorption features. These equivalent widths were measured in `cspec`, a program designed at the University of Minnesota to view 1D spectra in text file format and

take measurements on spectral features. Figures comparing emission and absorption profiles between the 2012 and 2018 epochs are normalized at the respective average continuum levels, and each region is referred to by its central wavelength. Multiple exposures existed for many of the regions, with varying integration times; frequently this was to capture features that were over- or under-exposed in a given spectrum. Differing spectra for a given epoch are noted within tables of equivalent width measurements where relevant.

Overall, we find that spectral features are weakening as we would expect, but at a significantly slower rate than previously identified in Mehner et al. (2010b). Changes in the emission profiles are small or negligible, while absorption features are consistently deepening. This tendency is seen across all four wavelength regions.

3.2.1 λ4706 Region

This wavelength region ranges from λ4561 to λ4841, and contains several blended emission features that were important in identifying the change in the wind density in 2010. As can be seen in Figure 3.3, there is qualitatively very little change in the profiles between 2012 and 2018, indicating that the weakening of the lines has slowed significantly. This qualitative behavior we observe in the lines is corroborated by the equivalent width measurements as listed in Table 3.1.

To ensure that the slowing rate of the changes was not simply a characteristic of the particular phase, we also compared spectra in this wavelength region at phase 2.20 (March 2010) to phase 3.20 (September 2015). Qualitatively, Figure 3.4 shows that compared to the dramatic changes observed between 1999 and 2010, the recent changes are nowhere near as rapid. Indeed, the lack of change is much closer to the modest spectral behavior observed between 1998 and 2004 (Mehner et al. 2010b, see also Figure 1.1).

In addition to the weakening of emission lines, we also observe a deepening of absorption features. This is particularly prevalent in the deepening of various P Cygni absorption profiles of He I, one of which occurs in this wavelength region (He I 4714; see Figure 3.5). P Cygni profiles arise when both absorption and

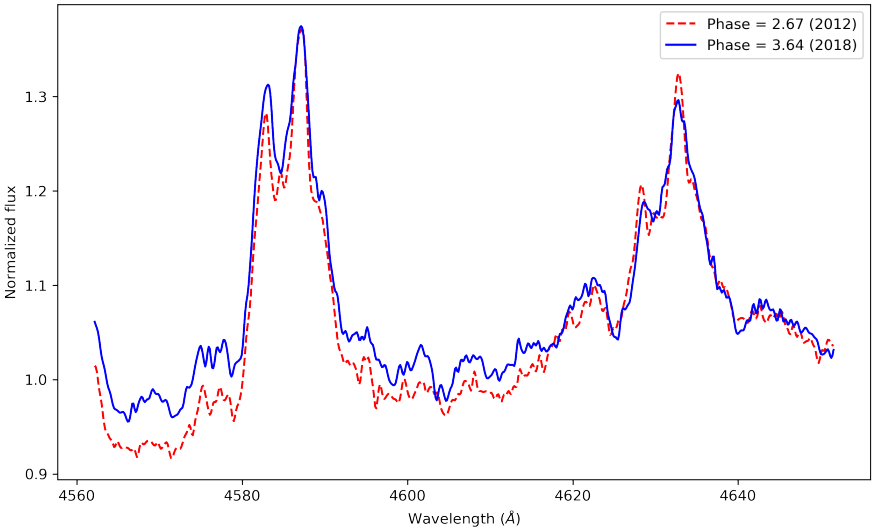

FIGURE 3.3: Blends of Fe II, [Fe II], Cr II, [Cr II], and N II as identified in Mehner et al. (2010b) and Davidson et al. (2015). Weakening of lines is barely noticeable at the 0.64-0.67 phase and seems to have slowed in this wavelength region overall since the findings in 2010.

emission exist in the profile of the same spectral line; the emission is from the stellar wind, while the absorption is a blueshifted feature of the outflowing material. The same decrease in density of the stellar wind is cited as the reasoning behind the deepening of these and other absorption profiles.

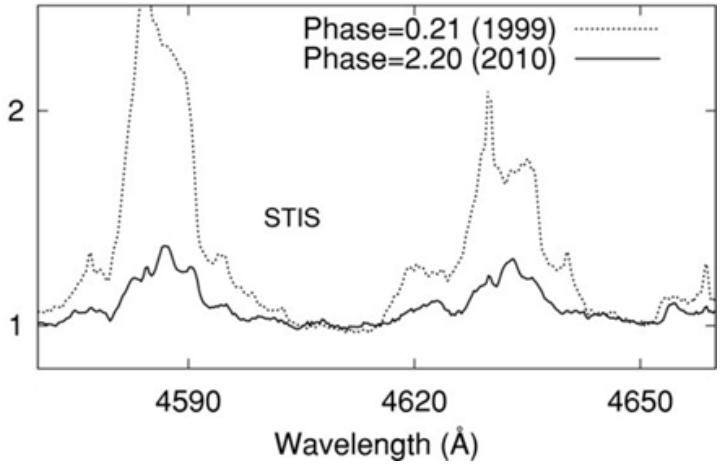

(A)

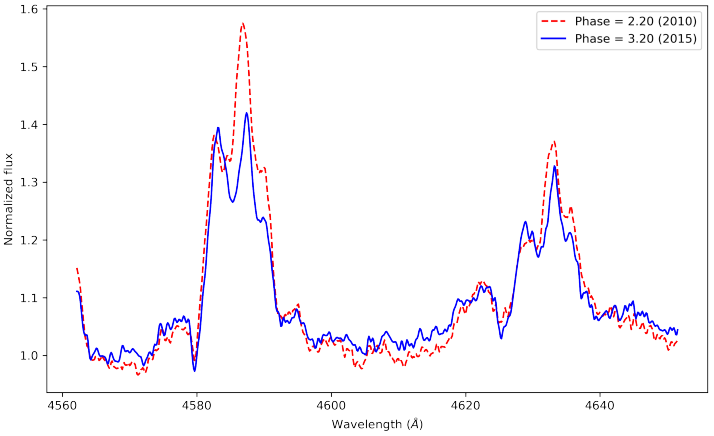

(B)

FIGURE 3.4: Comparison of the same blended features near 4600Å for the 0.2 phase. 3.4a is adapted from Mehner et al. (2010b), while 3.4b shows the same region at the same phase has not changed as dramatically in more recent years. This serves to show that the slowing rate of changes is not simply a characteristic of the phase of our newest 2018 data.

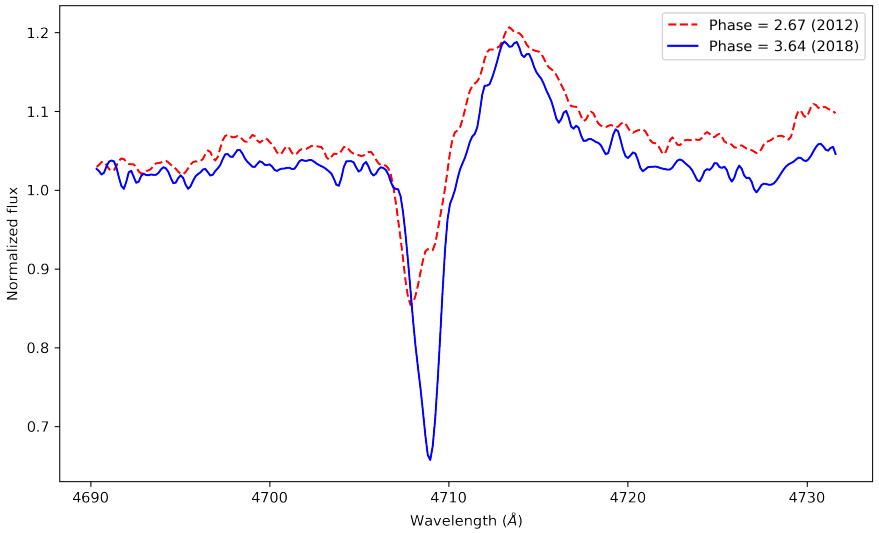

FIGURE 3.5: Distinct P Cygni profile for the He I 4714 spectral feature. Deepening of the blueshifted absorption profile between the two epochs due to the decrease in the stellar wind density is clear, while the emission profile shows the same small-to-no change as all other emission features between the two epochs.

Date	Phase	Continuum (erg/s/cm^2/Å)	EW (Fe II, Cr II)[a] (Å)	EW ([Fe II], N II)[b] (Å)	EW$_{abs}$ (He I 4714)[c] (Å)	EW (He I 4714)[d] (Å)
2012 Oct	2.67	1.340×10^{-11}	3.51	4.46	-0.31	0.85
2018 Feb	3.64	2.306×10^{-11}	2.97	3.51	-0.51	0.87
2010 Mar	2.20	1.260×10^{-11}	4.23	4.41	-0.41	0.65
2015 Sept	3.20	1.770×10^{-11}	3.61	3.94	-0.49	0.90

TABLE 3.1: Equivalent Widths of Stellar-Wind Emission and Absorption Features, λ4706 Region
[a]Measured between 4570-4600 Å
[b]Measured between 4613-4649 Å
[c]Measured between 4706-4710 Å
[d]Measured between 4710-4717 Å

3.2.2 λ5734 Region

This range covers λ5454 to λ6018. Of particular note are several N II absorption features as identified in Mehner et al. (2011), as well as the new developments of an unusual [N II] emission feature, as discussed below.

The N II absorption features ranging from 5668 Å to 5712 Å (vacuum wavelengths) are important for a variety of reasons. Firstly, they are a group of very few permitted N II lines that are strong and distinct enough to be observed; that is, they are not blended with other features such as the iron and chromium features in the 4600 Å region (Mehner et al. 2011). Like the P Cygni absorption profiles, the N II absorption is deepening over time, as can be seen in Figure 3.6. Prior to their 'discovery' in Mehner et al. (2011), these nitrogen lines were too weak to pick out from the continuum with confidence. These lines are likely produced in regions of the primary wind that are close to the secondary star (i.e., near zone 4 in Figure 1.3), which provides the UV photons necessary for N II generation (Mehner et al. 2011).

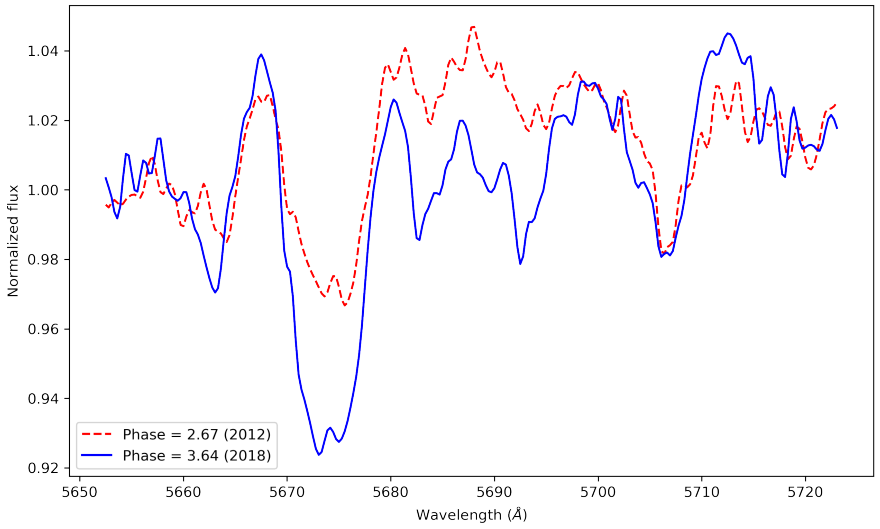

FIGURE 3.6: Clear deepening of N II absorption features, as identified in Mehner et al. (2011).

Of particular interest was a feature whose primary component is identified as [N II] λ5756[1], which has a vacuum wavelength of 5756.24 Å and is an electric quadrupole

[1]This feature is also sometimes referred to as [N II] λ5755.

transition of N II from the $2s^2 2p^2\ ^1S_0$ to $2s^2 2p^2\ ^1D_2$ level.[2] The primary peak around 5750.22 Å, strongly visible in the 2001 spectrum, is blueshifted in all three epochs by ∼6.02 Å, yielding a Doppler velocity of approximately -314 km/s. This is consistent with Doppler velocities measured for other nitrogen features both in the surrounding wavelength region and elsewhere (Mehner et al. 2011; Davidson et al. 2018). This particular feature arises from indirect photoexcitation via hydrogen-ionizing photons; see discussion in Davidson (1971) for further detail.

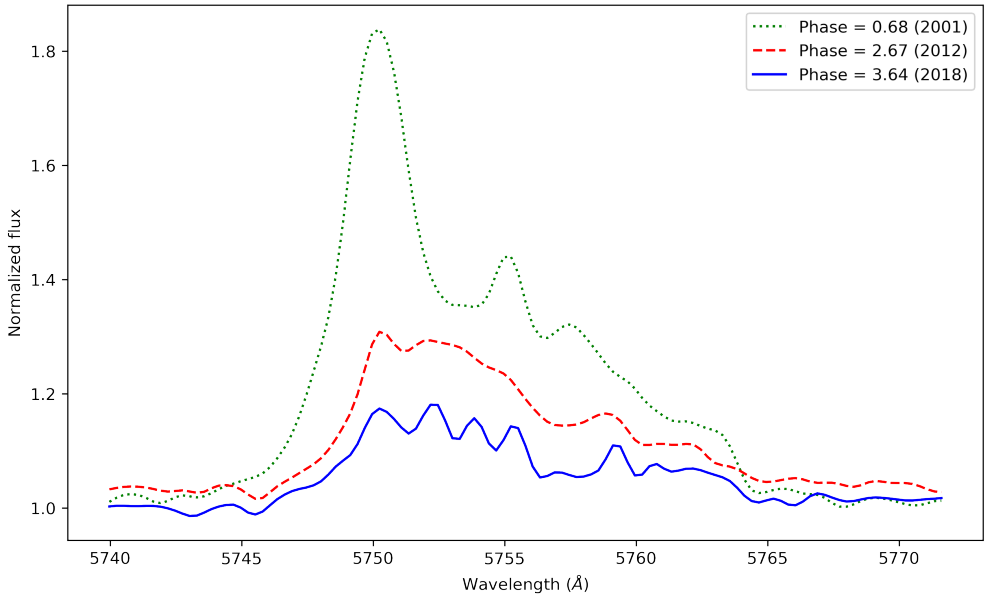

FIGURE 3.7: Development of the [N II] λ5756 profile over time. Distinct peaks are visible in the 2018 epoch that were not visible in earlier spectra. These peaks are almost certainly different velocity components of the same [N II] λ5756 species.

As we would expect, Figure 3.7 shows that [N II] λ5756 appears to be weakening as the mass loss rate decreases over time, except that additional peaks have resolved in the newest 2018 spectrum. This may be due to the decreasing density of the stellar wind, which could have "filled out" the regions in between peaks in previous spectra. These peaks are almost certainly different velocity components of the same [N II] species as opposed to a blend of species due to their similarity to other nitrogen features with analogous Doppler velocity profiles (see Davidson et al. 2018).

[2] Atomic Line List http://www.pa.uky.edu/∼peter/newpage/

Tracking this feature over the previous spectroscopic cycle shows significant variation of the profile throughout the course of the binary partner's orbit (see Figure 3.8). This wavelength region was not observed by the STIS/CCD between September 2013 and February 2018, so we use the previous cycle (cycle 2) for our analysis. The newest changes in the February 2018 spectra are still unique in comparison to all of the variation seen across the cycle, the latter of which is simply due to the changing position of the secondary star.

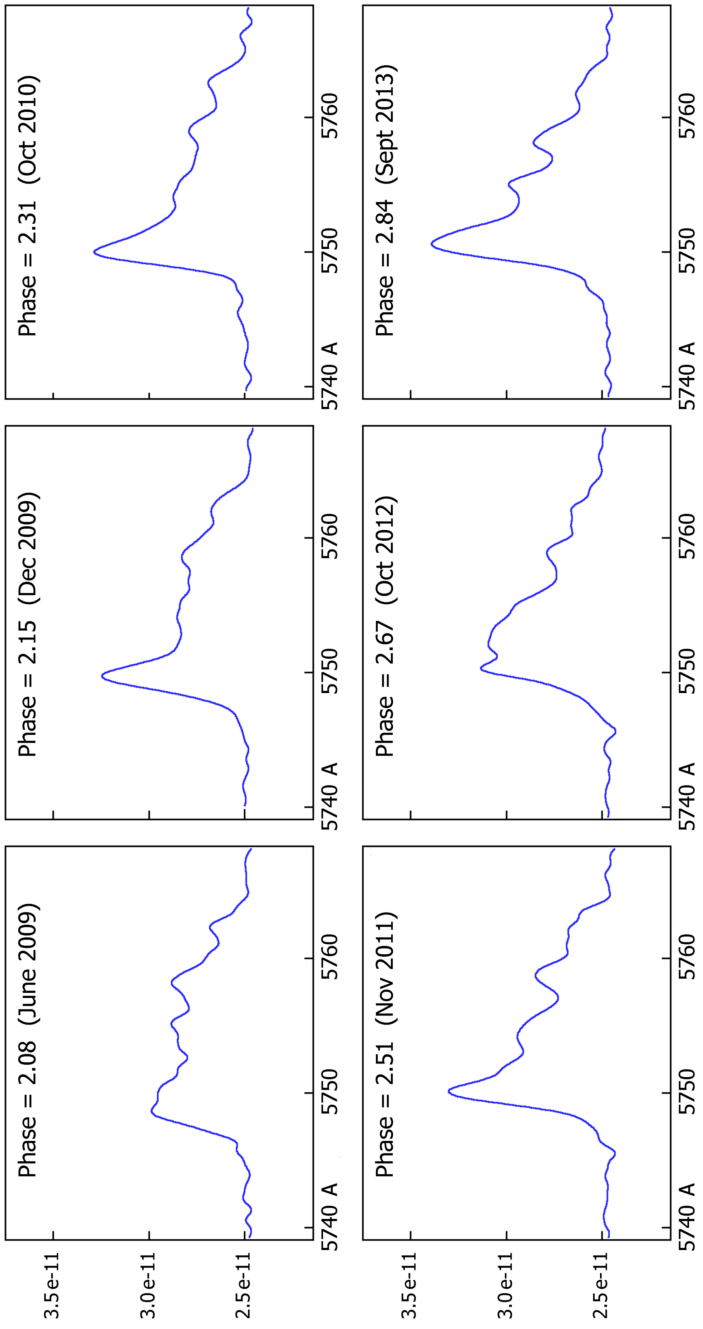

FIGURE 3.8: Variation of the [N II] λ5756 emission profile over the previous spectroscopic cycle (cycle 2). The decrease in strength of the line in the top left panel is due to its proximity to the 2009 spectroscopic event at periastron.

Date	Phase	Continuum (erg/s/cm^2/Å)	EW (Fe II blend)[a] (Å)	EW ([N II])[b] (Å)	EW$_{abs}$ (He I 5877)[c] (Å)	EW (He I 5877)[d] (Å)
2001 Oct	0.68	4.184×10^{-12}	4.07	5.78	-0.55	8.58
2012 Oct[e]	2.67	1.602×10^{-11}	1.69	2.63	-0.96	7.91
2012 Oct[f]	3.20	1.770×10^{-11}	1.59	2.28	...	...
2018 Feb	3.64	2.474×10^{-11}	1.12	1.70	-1.05	6.02

TABLE 3.2: Equivalent Widths of Stellar-Wind Emission and Absorption Features, λ5734 Region

[a]Measured between 5521-5546 Å

[b]Measured between 5745-5764 Å

[c]Measured between 5866-5870 Å

[d]Measured between 5870-5881 Å

[e] 5 second exposure time

[f]35 second exposure time; He I 5877 emission saturated

3.2.3 λ6768 Region

This region spans λ6488 to λ7052, and is centered at λ6768. This is most notably the region in which the Hα line is found. As can be seen in Figure 3.9, this profile has changed shape rather dramatically over time; the lack of difference in the profile between 2012 and 2018, therefore, is notable and further supports the trend of very small differences in the spectral emission features. The narrow absorption feature noted in Mehner et al. (2010b) is visible in the 2001 spectrum, and has not reappeared since. Hα is particularly important for a variety of reasons; because of the dense ionized wind surrounding the central star, the Hα-emitting region is thought to be significantly extended from the stellar radius (Wu et al. 2017). This has been used to test stellar wind models in Wu et al. (2017), and in this work, the STIS Hα EW measurements are used to make an estimate of the change in the stellar mass loss rate (see section 3.3).

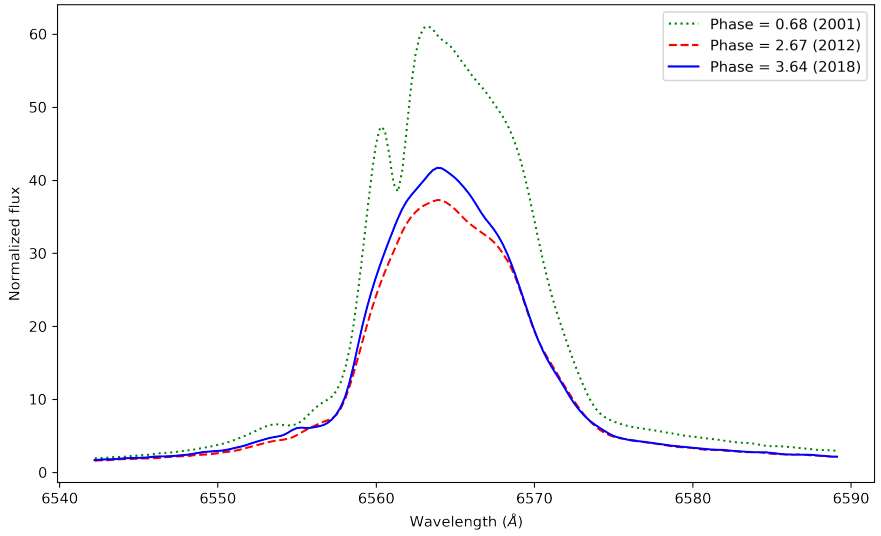

FIGURE 3.9: Hα emission profile for three epochs at the same phase: 2001, 2012, and 2018. The narrow absorption feature visible in the 2001 spectrum has not reappeared at this phase since being noted in Mehner et al. (2010b); little change in the shape of the profile has occured between 2012 and 2018.

Date	Phase	Continuum (erg/s/cm^2/Å)	EW (Hα)^a (Å)	EW$_{abs}$ (He I 6680)^b (Å)	EW (He I 6680)^c (Å)
2000 Oct	0.68	5.901×10^{-12}	763.35	...	...
2012 Oct	2.67	1.565×10^{-11}	469.01	-0.68	4.06
2018 Feb	3.64	2.250×10^{-11}	502.26	-0.82	4.69

TABLE 3.3: Equivalent Widths of Stellar-Wind Emission and Absorption Features, λ6768 Region
^{a}Measured between 6524-6608 Å
^{b}Measured between 6668-6672 Å
^{c}Measured between 6672-6684 Å

3.2.4 λ7283 Region

This region ranges from λ6999 to λ7563. It is relatively free of features compared to the other visible regions; the only two of note are the P Cygni profiles of He I 7067 and He I 7280.

The shift and change in shape of the He I 7067 profile (Figure 3.10) is due to the highly complex shape of the stellar wind zones, which change over the course of the secondary's orbit; this is still not well-understood (Mehner et al. 2011; Davidson et al. 2018). It is believed that the shape of the wind zones causes shifts in the velocity of this species, resulting in different velocity components that are more or less strong at any given point in the cycle. This is the most likely scenario for the changing shape of the emission profile of this feature.

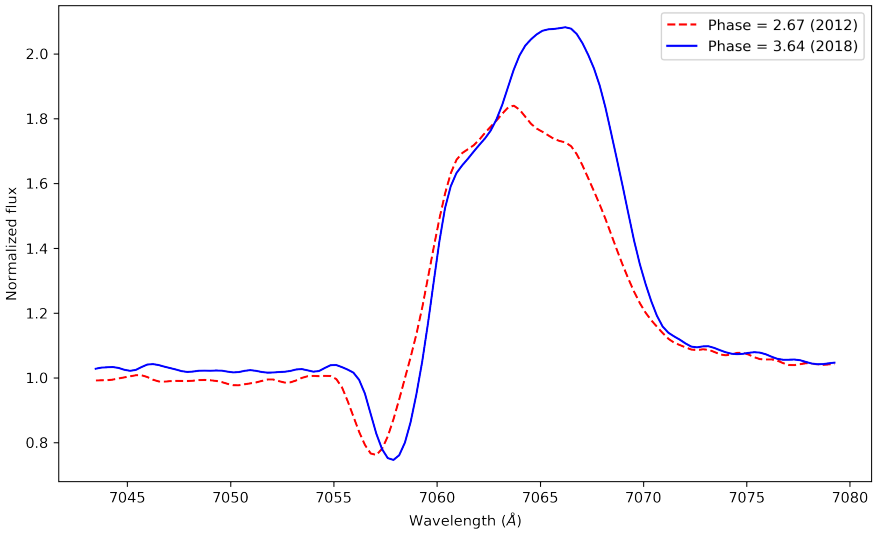

FIGURE 3.10: He I 7067 P Cygni profile, exhibiting a slight Doppler shift from 2012 as well as a change in the shape of the emission profile. The change in shape is likely due to differing strengths of various velocity components, which are a result of the complex shape of the stellar wind zones from which it arises.

Date	Phase	Continuum (erg/s/cm^2/Å)	EW$_{abs}$ (He I 7067)^a (Å)	EW (He I 7067)^b (Å)	EW$_{abs}$ (He I 7283)^c (Å)	EW (He I 7283)^d (Å)
2012 Oct	2.67	1.813×10^{-11}	-0.43	7.38	-0.18	1.40
2018 Feb	3.64	2.511×10^{-11}	-0.47	8.76	-0.25	1.51

TABLE 3.4: Equivalent Widths of Stellar-Wind Emission and Absorption Features, λ7283 Region
^{a}Measured between 7055-7058 Å
^{b}Measured between 7058-7072 Å
^{c}Measured between 7271-7275 Å
^{d}Measured between 7275-7288 Å

3.2.5 UV Regions

Though observations in the UV regions were available in this dataset, analysis of this region is beyond the scope of this work. This region is particularly complex and densely populated with hundreds of spectral features for which the continuum level is difficult or nearly impossible to determine (see Davidson et al. 2018 for further discussion of the UV Jungle, as well as Hillier et al. 2001). It is clear that like the visible regions, the UV is also brightening over time due to the expansion of the nebula and decrease in the stellar wind density; see Figure 3.11 for the UV light curve over time.

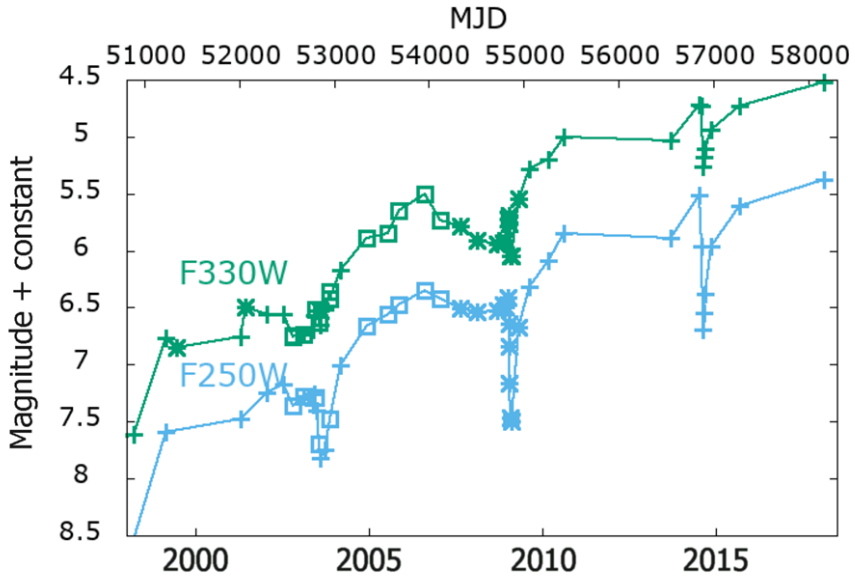

FIGURE 3.11: Light curve for Eta Car over time, showing the increase in UV brightness. Photometry based on NUV regions (F330W and F250W filters). Crosses (+) show synthetic photometry from STIS/CCD spectra near 3300Å and 2500Å, boxes (□) from ACS/HRC images, and asterisks (*) from WFPC2 images (see Martin et al. 2006b). Decreases in magnitude coincide with the periastron spectroscopic events. Plot courtesy of John Martin and Kris Davidson.

3.3 Mass Loss Rate

We know that the mass loss rate appears to be decreasing over time, but that change seems to have slowed in recent years, given the behavior of the emission

features described above. As in Mehner et al. (2012), we decided to make a crude estimate of the change in mass loss rate using methods from Leitherer (1988), which relate the Hα emission of the stellar wind to the mass loss rate $\dot{M}$. Equation (8) in Leitherer (1988) finds the relation to be

$$log(L(H\alpha)) = 2log|\dot{M}| - 2log(v_\infty) - log(R) + c(T_{eff}) + I + 25.125$$

where L(Hα) is the Hα luminosity in $L_\odot$, $\dot{M}$ is the mass loss rate in $M_\odot$/year, v_∞ is the terminal velocity of the stellar wind in km/s, R is the radius of the star in $R_\odot$, c(T_{eff}) is a temperature-dependent constant, and I is another value obtained from modelling related to the velocity law exponent (see Leitherer 1988, for further discussion and modelling of these latter two terms). Since we do not know parameters such as the temperature and radius of the primary star with certainty, we take a ratio between the two epochs to get the relative change. If we assume as in Mehner et al. (2012) that only the mass loss rate is responsible for the observed changes in the Hα flux, then we can simply take

$$\frac{log(L_{2018}(H\alpha))}{log(L_{2012}(H\alpha))} \approx \frac{log|\dot{M}_{2018}|}{log|\dot{M}_{2012}|}$$

Since the continuum-subtracted Hα flux is proportional to the equivalent width of the feature, we can simply use the values found in Table 3.3 to show that there has been little to no change in the mass loss rate over the past six years:

$$\frac{log|\dot{M}_{2018}|}{log|\dot{M}_{2012}|} \propto \frac{log(502.26)}{log(469.01)} = 1.011$$

This implies that the mass loss rate for the central star is still on the order of $\sim 10^{-3}$ $M_\odot$/year. This follows the trends indicated by the emission line features across all of the visible wavelength regions considered above, and contrasts with the decrease in mass loss rate by a factor of 2-3 that Mehner et al. (2012) obtained. The decrease in the wind density has clearly slowed since 2012.

CHAPTER 4: The Homunculus Nebula

4.1 Expansion Rate

If we assume that the expansion rate of the nebula is ballistic (i.e., linear) over the 18 year baseline, it is relatively easy to measure this value using the spectral data. In principle, all that needs to be done is to track the positions of bright clumps of gas over time, which appear as relatively brighter features in the continuum of the Homunculus spectra (see Figure 4.1). These positions correspond to discrete pixel row values in the spectrum, which we can determine using a variety of methods.

To this end, in collaboration with Dr. William Mitchell, Visiting Assistant Professor of Mathematics at Macalester College, we wrote a MATLAB program `specinterp` that interpolates a continuous function which nearly perfectly fits the intensity tracing data extracted using `exfits`. The full MATLAB program can be found in Appendix A. This program uses existing MATLAB code to perform a fast fourier transform (FFT) in combination with the open source MATLAB software `Chebfun`, which generates a polynomial interpolation via expansions in Chebyshev polynomials (Driscoll et al. 2014). We then differentiated this polynomial and found the roots; some of these roots are maxima corresponding to the peaks of features. These peaks are representative of a position along the slit (and in turn, the position of that bright clump of gas in the nebula). We selected as many features as we could, with the following criteria:

1. Features had to be reasonably well distinguished from their surroundings in both epochs.
2. Features had to be identifiable as the same feature in both epochs (based on shape of profile and pattern recognition).
3. We disregarded anything in the center portion of the spectrum, where direct light from the central star contaminates what we consider to be the brightness of the nebula (roughly rows 399 - 606 in the 2000 epoch, and rows 363 - 615 in 2018 epoch; see Figure 4.1).

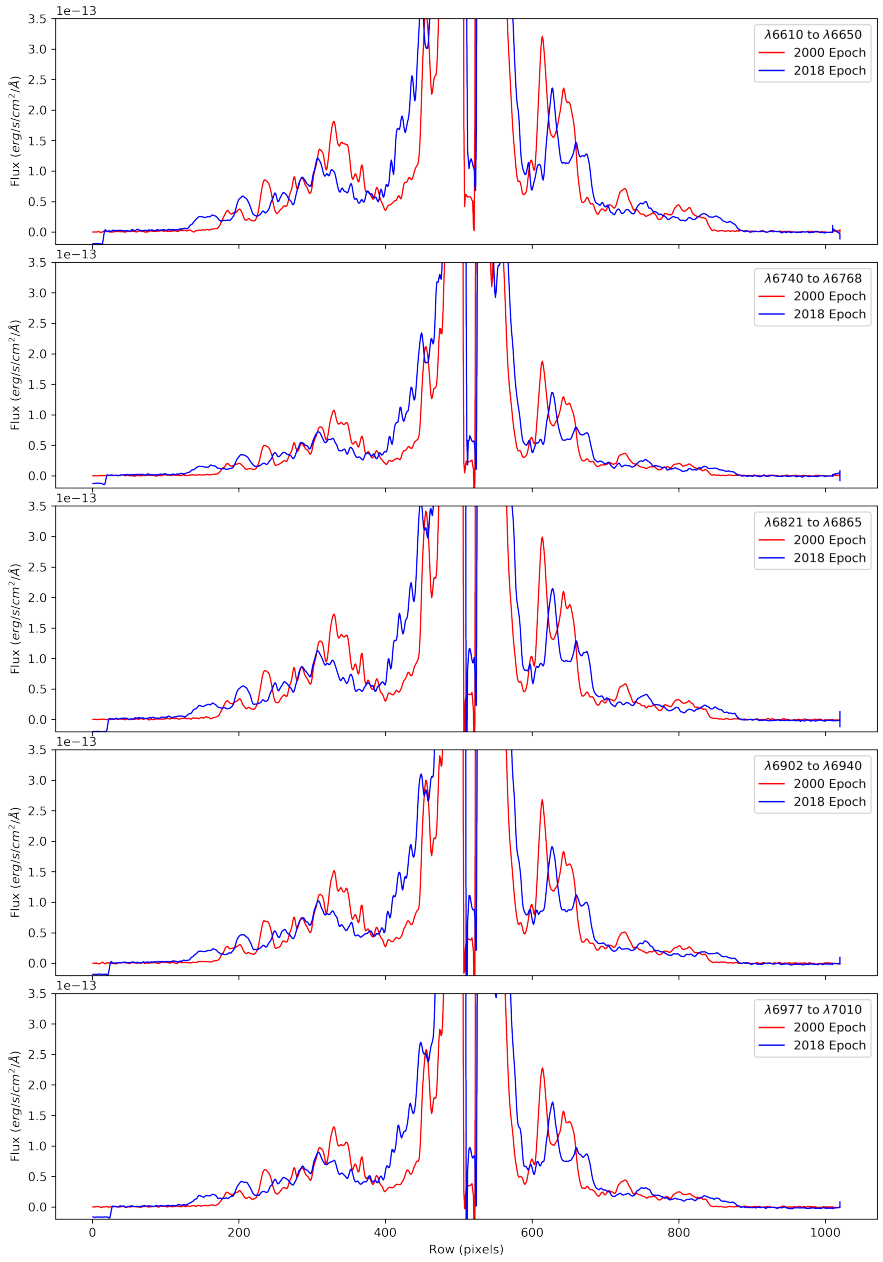

FIGURE 4.1: The five one-dimensional tracings extracted from the λ6768 region. These are representative of the continuum of the nebula, with bright clumps or knots of material appearing as peaked profiles. The left side of the tracing represents the SE lobe of the nebula, while the right is the NW lobe.

Some of these conditions, especially (2), could be automated using cross correlation software or other analogous pattern recognition or correlation techniques. For our purposes, the human eye was deemed sufficient to identify appropriate features. Twelve peaks were chosen to fit these criteria from the λλ6610−6650 region (8 from

the left SE lobe, 4 from the right NW lobe), and their positions were extracted for each epoch using the `specinterp` program; these positions are tabulated in Table 4.1 and plotted against one another in Figure 4.2. There is undoubtedly some systematic uncertainty in these values, as some of these features may be changing shape over time; the second of our selection criteria attempted to mitigate this issue.

2000 Peaks (pixel)	2018 Peaks (pixel)
199.61	163.17
234.26	204.04
274.63	248.36
284.81	259.77
309.07	285.50
328.48	306.49
366.77	351.85
387.34	374.26
641.96	658.78
725.60	754.18
798.51	834.27
813.59	850.04

TABLE 4.1: Peaks of Homunculus Continuum Features for Both Epochs

The two sets of peaks were then fit using a least squares method to determine a linear expansion rate between the two epochs. To ensure that the continuum was consistent across all extracted regions, this was repeated with a smaller set of peaks (6 peaks total, 4 left and 2 right) for the four other extractions. All values agreed with each other within their uncertainties, and overall had an average value of 11.8% with a standard deviation of 0.2%. These expansion rates are listed in Table 4.2.

λ Region	Expansion Rate (%)	$\pm$ Uncertainty (%)
6610 - 6650	11.9	$\pm$0.1
6740 - 6768	11.9	$\pm$0.1
6821 - 6865	11.8	$\pm$0.4
6902 - 6940	11.5	$\pm$0.4
6977 - 7010	12.1	$\pm$0.2

TABLE 4.2: Expansion Rates for Homunculus Continuum Regions

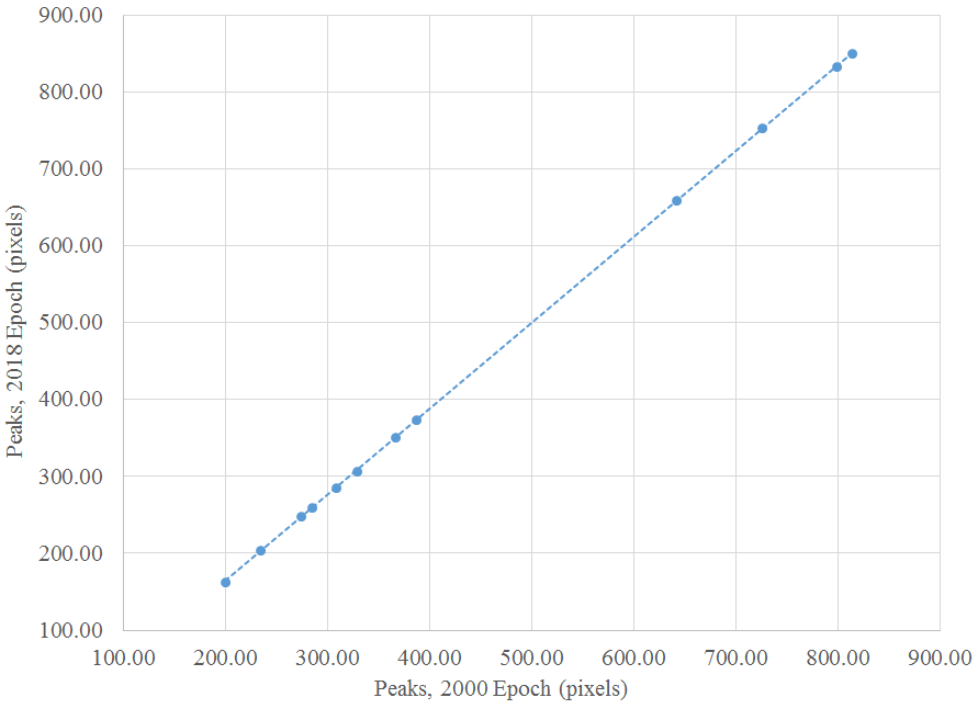

FIGURE 4.2: Plot of the positions of the peaks of continuum features for both 2000 and 2018 epochs, the best fit line of which represents the expansion rate over the 18 year baseline. Peak values listed in Table 4.1.

We also plotted peak values against the difference between the two positions to see how much deviation from an expected difference there was. The expected difference is derived from a best fit line, which represents the expansion rate of 11.9%. The resulting plot is seen in Figure 4.3, which shows very little deviation from an expected difference in position. Looking at the expected difference and the measured difference (Figure 4.4), we can see that the spread of the difference between these two values is quite small.

Because of the excellent correlation of the points, we can assume that the peaks we selected are all from the lobes of the main Homunculus, and that our assumption of a linear rate of expansion is reasonable. The former is sensible, as the Little Homunculus likely does not extend beyond the bright section in the central portion of the spectra, which was explicitly avoided in our selection of peaks (see Figure 4.5 for the extent of the Little Homunculus). This also indicates that none of the features selected are bright knots of gas that are moving at atypical rates from their surrounds.

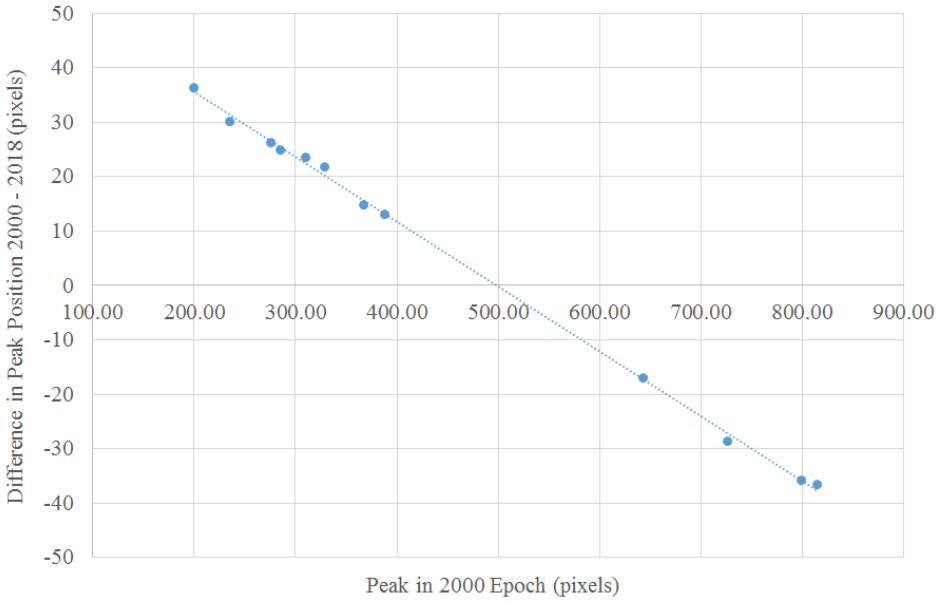

FIGURE 4.3: Plot of the difference between continuum feature peaks (i.e., the proper motion of peaks as they expand over time). The best fit line represents the expected difference based on the expansion rate of 11.9%. Deviations from this fit are present, but they are quite small (see Figure 4.4).

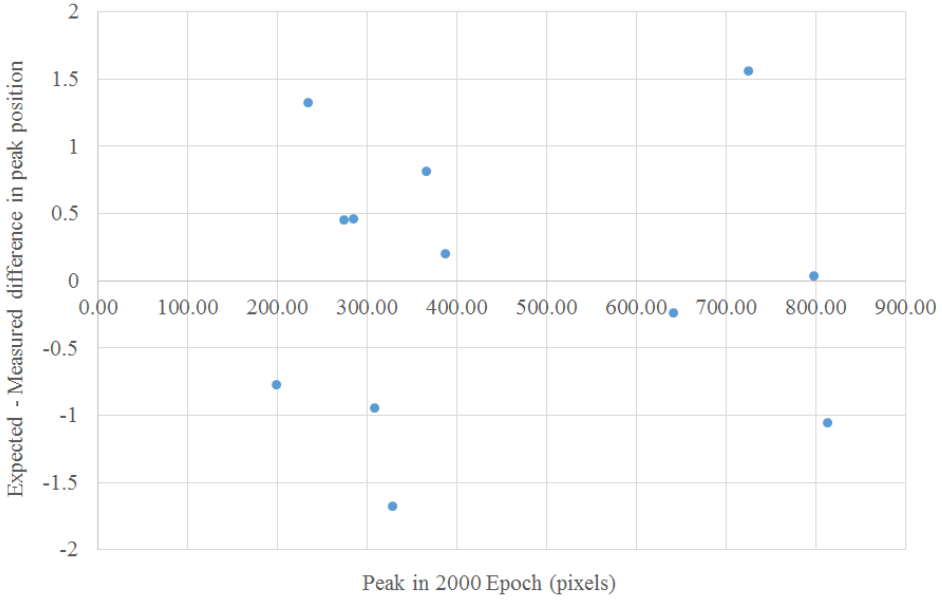

FIGURE 4.4: Plot of expected - measured difference between continuum feature peaks. The relatively small spread shows that most of the measured differences between the peak positions are very close to what we would expect from the best fit. The assumption of a linear expansion is thus quite reasonable.

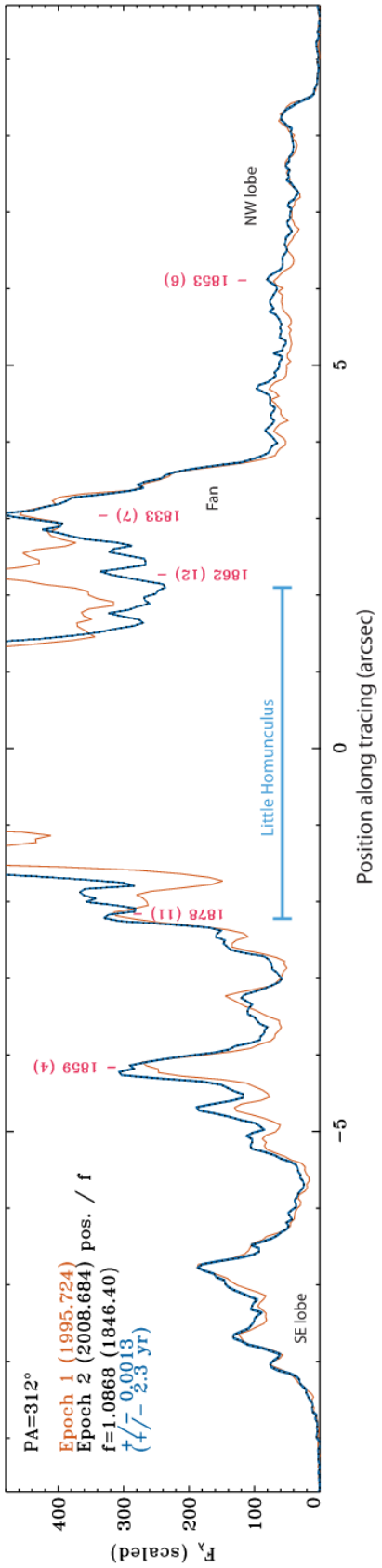

FIGURE 4.5: Homunculus nebula *HST*/WFPC2 intensity tracing for a position angle with similar slit orientation as our data. The light blue bar at the bottom shows the extent of the Little Homunculus in the tracing; note that it is contained within the brightest central regions. Epochs are scaled by both position and intensity. Adapted from Figure 3 in Smith (2017).

4.2 Age of the Nebula

Using this expansion rate, we can do a rudimentary calculation in order to determine the age of the Homunculus overall. Taking the difference between the dates of observation,

$2018.156 - 2000.199 = 17.957$ years

and dividing this by the expansion rate, 0.119, yields 150.9 ± 1.7 year, which corresponds to an initial ejection date of 1849.2 ± 1.7yr (mid March, 1849). This is within uncertainties of the dynamical age of the nebula determined by Smith (2017) and Morse et al. (2001). Because these values agree within uncertainties and were derived from differing methods and data, this corroborates our values as a valid estimate for the time of the eruption.

4.3 Brightness Ratios

In order to more easily examine the brightness ratio of the two epochs, it is sensible to scale the 2018 epoch by the inverse of the expansion rate such that the nebular structure corresponds with the same range of pixels as the 2000 epoch. This scaled view is shown for the $\lambda\lambda$6610-6650 region in Figure 4.6.

The Homunculus is a reflection nebula, referring to the fact that it is not self-luminous but instead reflects the light from the central star. Because the nebula is expanding over time, we expect it to decrease in brightness, since a decrease in density enables light from the star to escape on direct paths outwards rather than reflecting off of the nebular material. This is indeed what we see in the left and rightmost portions of the tracings in Figure 4.6; near the center, we see some brightening effects due to the central star's increase in flux, but in the areas corresponding to the lobes of the nebula, the brightness has decreased over time. On the left side of the central region (near ∼400-450 pixels), we can see that new, bright features appear to be moving outwards in the 2018 epoch, likely from the expansion of the Little Homunculus. The asymmetry is likely due to the inclination of the system with respect to our line of sight.

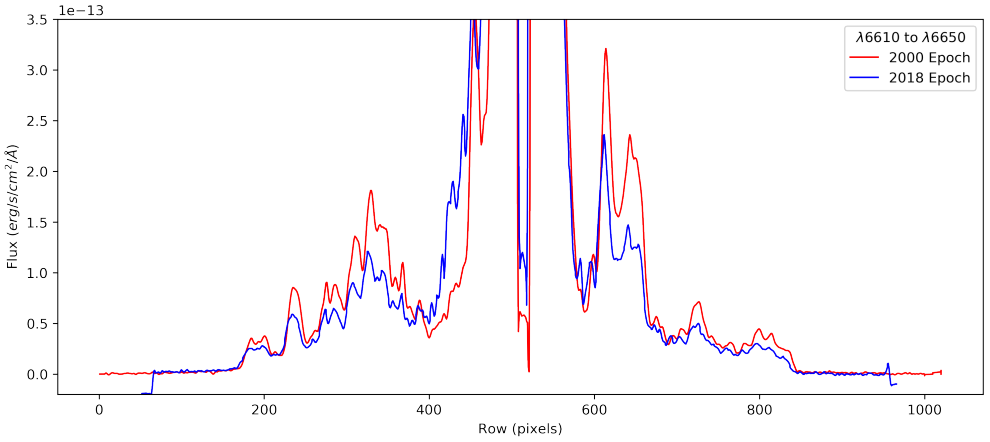

FIGURE 4.6: Homunculus continuum tracing for the $\lambda\lambda$6610-6650 region, with the 2018 epoch scaled by a factor of 0.893 and horizontally shifted by a small arbitrary constant. This allows us to better probe the relative intensity of the continuum for these epochs.

This decrease in brightness is also measured in the mid-IR; Morris et al. (2017) find a 25% decline in brightness between the 1970s and 2017.

CHAPTER 5: Conclusions

We find that the central star seems to have settled back into a state of slow, secular change rather than the heightened rate of change that occurred between approximately 2004 and 2010. This is represented both qualitatively by the shapes of the spectral line profiles, as well as quantitatively by their measured equivalent widths. This trend is seen consistently across all visual wavelength regions available in this dataset. An estimate of the change in mass loss rate yields little to no difference over the course of 6 years, further supporting the explanation of a decrease in stellar wind density. Continuing to track these trends is of prime importance for as long as the *HST*/STIS instrument remains available for science.

Using intensity tracings of the Homunculus and an interpolation program to track the motions of bright clumps of gas, the nebula appears to behave as we expect in terms of a linear/ballistic expansion. Our expansion rate of 11.9% ± 0.1% yields an ejection date of 1849.2 ± 1.7 yr, which agrees within uncertainties with recent studies (Smith 2017; Morse et al. 2001), and the lobes of the nebula are decreasing in brightness as the expansion continues over time. Future work would be to investigate other wavelength regions for the continuum of the Homunculus, assuming that we could acquire deeper integrations of regions where there was little to no emission or absorption features to interfere. Having a measurement of the expansion rate using other wavelength regions would ensure that our values are not systematically affected based on the wavelength region we used. Agreement in the ejection date indicates that any such issues would be minimal, but nevertheless, it would provide an even stronger corroboration of our results.

Uncovering the history of the system through increasingly precise measurements of the expansion rate and ejection date of the Homunculus nebula is of particular importance. Through understanding its expansion and ejection physics, the Homunculus can yield insight into both bipolar mass loss and the nature of pre-supernova ejections in massive stars. Knowing the timeline of the ejection also helps us interpret the myriad other historical data that exists for Eta Carinae.

Our work continues the decades-long effort to track the behavior of the Eta Carinae system as a whole. Understanding the recovery of this object from its nonterminal explosion will lend critical insight into the late stages of evolution for potentially similar objects, some of which have already been identified in other nearby galaxies. Studying Eta Car in tandem with these new analogs will help us to know if Eta Car is truly unique or, as is more likely, whether Eta Car's behaviors are also exhibited by other extremely massive stars. Tracking Eta Car's behavior over time will allow for the prediction of future trends in both its own system and others, including when and how it will eventually die.

Work on the central star was completed as a part of the summer 2018 University of Minnesota Physics and Astronomy REU Program, funded by the National Science Foundation. This work has made use of the data archive for Eta Carinae, which is available online at http://etacar.umn.edu. The archive is supported by the University of Minnesota and the Space Telescope Science Institute under contract with NASA.

APPENDIX A: spectrainterp.m Program

```
% Program written by Dr. William Mitchell and Greta Helmel; all comments by
% Greta Helmel. This code interpolates a continuous function based on
% spectral data points provided in text file format, such that local maxima
% and minima can be mathematically determined but selected for using human
% discretion.

% Load in the spectral data
load filename.txt
t00 = filename(:,1); % x value (in our case, pixel values or rows)
f00 = filename(:,2); % flux values

% Perform a Fast Fourier Transform on the data
NC = length(t00);
xc = linspace(0,2*pi*((NC-1)/NC),NC);
yc = f00
c = fft(yc);
c_shift = fftshift(c);
yf = 0;
if mod(NC,2)==0
    st = -NC/2;
    en = -st - 1;
else
    st = -(NC-1)/2;
    en = -st;
end
freq = st:en;
xf = chebpts(10000,[0,2*pi]);

for j = 1:NC
    yf = yf + c_shift(j)*exp(1j*freq(j)*xf)/NC;
end
```

```
% Create the smooth function that represents the data
u = real(chebfun(yf,[0,2*pi]));

% Plot the original data, the smooth function, and the roots
clf
hold on
plot(xc,yc,'bo')
plot(xf,real(yf),'g.')
p1 = roots(diff(u));
plot(p1,u(p1),'rs');

% View numerical values for the maxima and minima on the plot
caption = num2str(p1);
text(p1,u(p1),caption,'Fontsize',10);}
```

APPENDIX A: Bibliography

Damineli, A. 2008, in Revista Mexicana de Astronomia y Astrofisica, vol. 27, Vol. 33, Revista Mexicana de Astronomia y Astrofisica Conference Series, 129–131

Damineli, A., Conti, P. S., & Lopes, D. F. 1997, , 2, 107

Davidson, K. 1971, MNRAS, 154, 415

Davidson, K., & Humphreys, R. M., eds. 2012, Astrophysics and Space Science Library, Vol. 384, Eta Carinae and the Supernova Impostors

Davidson, K., Ishibashi, K., Martin, J. C., & Humphreys, R. M. 2018, ApJ, 858, 109

Davidson, K., Mehner, A., Humphreys, R. M., Martin, J. C., & Ishibashi, K. 2015, ApJ, 801, L15

Driscoll, T., Hale, N., & Trefethen, L. 2014, Chebfun Guide, 1st edition, Pafnuty Publications

Gull, T. R. 2007, in Astronomical Society of the Pacific Conference Series, Vol. 367, Massive Stars in Interactive Binaries, ed. N. St.-Louis & A. F. J. Moffat, 263

Hernandez, S., & et al. 2012, Space Telescope Imaging Spectrograph Instrument Handbook for Cycle 21 v. 12.0

Hillier, D. J., Davidson, K., Ishibashi, K., & Gull, T. 2001, ApJ, 553, 837

Hofmann, K. H., & Weigelt, G. 1988, A&A, 203, L21

Ishibashi, K., Gull, T. R., Davidson, K., et al. 2003, AJ, 125, 3222

Kashi, A., & Soker, N. 2010, ApJ, 723, 602

Khan, R., Adams, S. M., Stanek, K. Z., Kochanek, C. S., & Sonneborn, G. 2015, ApJ, 815, L18

Kiminki, M. M., Reiter, M., & Smith, N. 2016, MNRAS, 463, 845

Leitherer, C. 1988, ApJ, 326, 356

Martin, J. C., Davidson, K., Humphreys, R. M., Hillier, D. J., & Ishibashi, K. 2006a, ApJ, 640, 474

Martin, J. C., Davidson, K., Humphreys, R. M., & Mehner, A. 2010, AJ, 139, 2056

Martin, J. C., Davidson, K., & Koppelman, M. D. 2006b, AJ, 132, 2717

Mehner, A., Davidson, K., & Ferland, G. J. 2011, ApJ, 737, 70

Mehner, A., Davidson, K., Ferland, G. J., & Humphreys, R. M. 2010a, ApJ, 710, 729

Mehner, A., Davidson, K., Humphreys, R. M., et al. 2012, ApJ, 751, 73

—. 2010b, ApJ, 717, L22

—. 2015, A&A, 578, A122

Morris, P. W., Gull, T. R., Hillier, D. J., et al. 2017, ApJ, 842, 79

Morse, J. A., Davidson, K., Bally, J., et al. 1998, AJ, 116, 2443

Morse, J. A., Kellogg, J. R., Bally, J., et al. 2001, ApJ, 548, L207

Smith, N. 2008, Nature, 455, 201

—. 2017, MNRAS, 471, 4465

Smith, N., & Frew, D. J. 2011, MNRAS, 415, 2009

Weigelt, G., & Ebersberger, J. 1986, A&A, 163, L5

Wu, Y.-L., Smith, N., Close, L. M., Males, J. R., & Morzinski, K. M. 2017, ApJ, 841, L7